Research Article
Hittite Journal of Science and Engineering, 2023, 10 (3) 269–277
ISSN NUMBER: 2148–4171
DOI: 10.17350/HJSE19030000316

Simultaneous Effect of Welding Current with Post-Weld T6 Heat Treatment on Corrosion Susceptibility of Al6013 Alloy Joined by GTAW

Mehmet Topuz
Van Yuzuncu Yıl University, Department of Mechanical Engineering, Van, Türkiye

ABSTRACT

Al6013 base metals were joined successfully with ER4047 filler metal by using the GTAW method under different welding currents. Post-weld T6 heat treatment effects on corrosion properties were investigated in terms of open circuit potential (OCP), potentiodynamic polarization (PDS), and electrochemical impedance spectroscopy (EIS) tests. It was determined that corrosion resistance of the post-weld samples increased with increasing welding current, while T6 heat treatment only effective on 110A and 140A welding current samples (3.61 to 2.08, 2.95 to 2.40, and 1.38 to 2.15 $\mu A \cdot cm^{-2}$ for 110A, 140A, and 170A welding current before and after T6 heat treatment). The characteristics of the oxide films on the surfaces are revealed with EIS analysis. While the passive film originating from Al is generated on the surfaces, the two-constant equivalent circuit model found that as it also contains pittings on the surface. It was determined that the pitting resistance of the T6 heat treated 110A sample increased (3075 to 4562 Ω). Post-corrosion SEM surface morphologies showed that low welding currents lead to more destruction as increased exposure to corrosion.

Keywords:
Al6013, GTAW, Weld current, T6 heat treatment, Corrosion

Article History:
Received: 2023/06/12
Accepted: 2023/07/31
Online: 2023/09/30

***Correspondence to**: Mehmet Topuz,*
E-mail: mehmettopuz@yyu.edu.tr;
Phone: +90 506 674 3546;
Fax: +90 432 225 1730

This article has been checked for similarity.

Introduction

Aluminium (Al), which second-largest subterranean reserve in the world, can exhibit different physical and mechanical properties as a result of various alloying and different heat treatment processes [1]. Because of the low density, simplicity in shaping, high corrosion resistance, and adaptable physical and mechanical properties of Al alloys, application fields are increasing day by day. These fields are in various fields such as the manufacturing industry, agriculture, energy, construction, and especially transportation [2]. The density value of Al is about 2.7 $g.cm^{-3}$, and it is about one-third of the density of steel (7.83 $g.cm^{-3}$) and copper (8.93 $g.cm^{-3}$), so it is favourable for weight reducing for vehicles such as airplanes or many others. As a result of the weight reduction due to its low density, it also contributes to the reduction of carbon emission in the aviation field so they have a significant place in the aerospace industries [3,4].

Today, there are numerous Al alloys developed for industrial applications [5]. High mechanical properties can be attained in such a vast number of Al alloys, particularly for alloys that can be heat treated following the age hardening procedure. 2XXX (Al-Cu), 6XXX (Al-Mg-Si), and 7XXX (Al-Zn-Mg) series Al alloys are favourable among these Al alloys for obtaining high mechanical properties after the aging process [6,7]. As a result of secondary aging heat treatment (T4: natural aging or T6: artificial aging) processes to be applied to these alloys, the strength of these Al alloys can be increased with a precipitation hardening mechanism [8,9]. This principle was discovered independently in 1938 by Guinier and Preston. It is based on the homogeneous dissolution of elements such as Cu, Mg, and Si in the alloy during solid solution and forming a precipitate with quenching [10]. Among these Al alloys, the 6XXX series, which is frequently used in the aerospace industry, stands out due to its relatively high specific strength as well as good formability, weldability, and corrosion resistance. Despite the mentioned benefits, the corrosion resistance of 6XXX alloys may decrease due to the alloying elements which increased impurity (percent decrease in the amount of Al). Therefore, studies on the development of 6XXX series Al alloy based on the investigation of heat treatment parameters have gained momentum [11]. 6XXX series alloys comprise Mg and

Cite as:
Topuz M, "Simultaneous Effect of Welding Current with Post-Weld T6 Heat Treatment on Corrosion Susceptibility of Al6013 Alloy Joined by GTAW" Hittite Journal of Science and Engineering, 10(3):269–277, 2023. doi:10.17350/hjse19030000316

Si that will form magnesium silicide (Mg_2Si) in their microstructure so precipitation hardening was favourable with heat treatment. The amount and size of Mg_2Si particles can vary depending on the temperature and time during the heat treatment [10]. When the T6 heat treatment is applied to the alloys in this group, the strength of the alloys can be increased remarkably. In addition to these two elements, 6XXX series may contain small amounts of Copper (Cu), Manganese (Mn), and other elements [12]. By adding Manganese (Mn) and Chromium (Cr) to many of the 6XXX series aluminium alloys, an increase in elastic limits and grain size control can be achieved. As a result, the relatively new alloy Al6013 has a higher Cu content than other 6XXX series, which improves its strength as a result of its secondary hardening mechanism [8]. Due to its high Cu concentration it tends to form precipitation-free zones (PFZ) at grain boundaries during precipitation hardening, which makes highly susceptible to intergranular corrosion the Al6013 alloy [13]. Al6013-T6 alloy has been popular in the aerospace, particularly because of its enhanced weldability and high resistance to corrosion [7].

Al6013-T6 alloy has good corrosion resistance during contact with different corrosive environments (air, water, oils, etc.) and against many other chemicals like all Al and its alloys [14]. Due to the high affinity of Al for oxygen, the thin and dense oxide layer (Al_2O_3) formed on the surface as a result of contact with the atmosphere provides resistance against corrosive effects. This feature of aluminium provides higher corrosion resistance as well as expanded its application area. The ability of aluminium to resist corrosion is directly related to its purity. In other words, other elements such as Mg, Si, Cu, etc., may be responsible for diminished corrosion resistance [15]. Therefore, it is necessary to investigate the corrosion behaviour of Al and its alloys in all processes.

In various applications, the use of welding, which creates joins of the same and/or different metals, becomes necessary [2,16]. Especially in industries such as aviation, it is important to joints multiple small and complex parts. Among various welding methods Gas Tungsten Arc Welding (GTAW) was mostly used because of applicable of wide range of applications. In GTAW method, a tungsten electrode carried by a suitable torch creates an arc with the base metal. High amount of heat was released as a result of this arc followed by base metal and filler metal melting [15]. The advantages of GTAW welding can be listed as follows; i) it can be applied with both manual and automatic welding systems, ii) it can be used by melting the base metal or melting an additional filler metal, iii) suitable for welding thin materials, iv) high penetration and non-porous joining can be made, v) the deformation of the workpiece is less since the heat input is concentrated on the weld zone, and vi) it gives a smooth weld seam [2,15]. The shielding gas sent to the welding area through the hood. Thus, possible welding faults are prevented by protecting the area. The shielding gas has a great influence on the stability of the arc and the quality of the weld [17].

There are various studies on the corrosion susceptibility of 6XXX series Al alloys. In the study conducted by Abo Zeid [18], the highest corrosion resistance was determined in the Al6013-T6 alloy. It was also stated that the Mg_2Si particles precipitated in the 6XXX series increased the corrosion resistance, especially the pitting corrosion. On the other hand, Lei et al. [13] have researched that T6 heat treatment parameters and the effect of different continuous heating at 20, 30, 40, 60, and 80 $^{o}C.min^{-1}$ on the microstructure, mechanical and corrosion properties of Al6013 alloy after 30 minutes of solution at 570 ^{o}C. However, with increasing final heat treatment temperature changes (140, 190, 220, and 240 ^{o}C) at a constant aging rate of 60 $^{o}C.min^{-1}$, it was determined that the intergranular corrosion depth decreased with increasing final heat treatment temperature. By this way, it has been predicted that the T6 heat treatment of the Al6013 alloy can inhibit corrosion, especially by reducing the intergranular corrosion mechanism with continuous heating. Furthermore, observation of intergranular corrosion at the cross-section of alloy has been proven together with the corrosion current density (I_{corr}) values and it has been revealed that maximum corrosion protection is obtained with continuous heating at 60 $^{o}C.min^{-1}$.

Al6013 alloy is a relatively new alloy specially designed for the aerospace industry, which was developed to increase the low yield and tensile stresses of the Al6061 alloy and to have similar mass properties [19]. However, compared to Al6061 alloy, its weldability remains low due to the insufficient Al proportion. According to the previous studies, the effect of welding current and post-weld T6 heat treatment was not investigated in terms of Al6013 alloy joined with the GTAW process. As a research hypothesis, corrosion susceptibilities can resemble those achieved with high welding current when T6 heat treatment is applied to an Al6013 alloy joint with low welding current strength. To put forward this hypothesis, Al6013 plates were joined by GTAW using ER4047 (AlSi12) alloy as filler metal, and after being characterized, corrosive properties were investigated in detail.

MATERIAL AND METHODS

Materials and GTAW Process

The extruded Al6013 alloy was supplied with the dimensions of 200×60×5 mm from Simitçioğlu Metal. AlSi12 (ER4047) alloy with a diameter of 3 mm was used as the filler metal (Blueweld GTAW AlSi12, Vega Makina). ER4047 alloy chosen for its advantages such as good flu-

idity, low melting point, enhanced corrosion resistance, and prevention of welding distortion after process. The chemical compositions of the Al6013 and ER4047 used along with the study were presented in Table 1. For the welding process, the parts to be welded were chamfered at 45 degrees and a pool was formed for the weld seam. Thus, two single v-grooves (Fig. 1a) were welded [5], and the effect of T6 heat treatment on welded plates was investigated. Zenweld Ultimate AC/DC 315 welding machine was used in GTAW processes, and welding currents were preferred as 110A, 140A, and 170A (A: Amperes), respectively. These currents were determined from detailed literature research for evaluating low, medium, and high welding current on welding process [2,20]. In addition, according to previous [1,17,20,21] and preliminary studies, other parameters were fixed as welding speed: 160 to 180 $mm.min^{-1}$, wire speed: 6 $mm.min^{-1}$, voltage: 20 V, and gas flow: 12 $L.min^{-1}$. During the GTAW of plates, 99.999% high-purity Ar gas was used as shielding gas for a protective atmosphere. The plates after the GTAW process, which were welded in 3 different currents, were cut into two with an abrasive cutter (Micracut 202, Metkon). Solutionizing was carried out at 575 °C for 1 h followed by quenched in ice water, T6 heat treatment was applied in a furnace (MT1120, Magmatherm) at 191 °C for 4 h [22]. After T6 heat treatment, the weld joints were cut into different sizes for further tests and analyses. To better clarification of the post-weld and T6 heat treatment processes in the joints, 110A, 140A, and 170A represents post weld joints while HT-110A, HT-140A, and HT-170A represents T6 heat treated joints after GTAW, respectively.

Table 1. Compositions of Al6013 and ER4047 alloys

Material	*Composition (wt.%)*								
	Si	*Ti*	*Zn*	*Cu*	*Fe*	*Mn*	*Cr*	*Mg*	*Al*
Al6013	*0.20*	*0.15*	*0.25*	*4.30*	*0.30*	*0.60*	*0.10*	*1.50*	*Balance*
ER4047	*12.00*	*0.05*	*0.10*	*0.05*	*0.50*	*0.15*	*-*	*0.05*	*Balance*

Microstructure Analysis

Before electrochemical corrosion tests of the weld zones (WZ: a combination of base metal, heat affected zone: HAZ, and weld seam), were characterized with macro photos. HAZs and weld seams were also characterized by optical microscopy (OM) images. NaOH etching was used for OM micrographs of welded joints. The before and after corrosion tests WZs were characterized by scanning electron microscopy (SEM) images and attached energy dispersive X-ray (EDX) analyses to detect both elemental analyses and the damages in the WZs after electrochemical corrosion tests. For precipitation formation at WZ was determined using X-ray diffraction (XRD, PANalytical Empyrean). XRD analyses were performed with a Cu-Kα radiation source at a wavelength of 1.5406 (angle range from 30 to 80 2θ) and a step rate of 0.05.

Electrochemical Corrosion Tests

The evaluation of the corrosion susceptibilities of WZ was carried out using Gamry PCI14/750 device following ASTM G59 standards [23]. Electrochemical corrosion tests were performed using the three-electrode method, Ag/AgCl and platinum were used as reference electrodes and counter electrode, respectively, while WZ was used as working electrodes. 3.5 by wt.% NaCl was used as the electrolyte and the WZ which was in contact with the electrolyte was fixed at 2 cm^2 and masked by cold moulding. The potential (E_{ocp}) changes were recorded in the electrolyte for 3600 s for the samples to reach the equilibrium state (open circuit potential: OCP). Then, the samples that reached the equilibrium state were polarized to ~0.15V vs. E_{ocp} starting from -0.3 V vs. E_{ocp} cathodic overpotential using 1 $mV.s^{-1}$ scanning rate with potentiodynamic scanning (PDS) method. Electrochemical impedance spectroscopy (EIS) measurements [24], especially for the oxide film forming ability of the WZ and the corrosion mechanism, are used with AC amplitude of 10 mV over OCP in the frequency range from 100 kHz to 0.01 Hz after PDS tests. Fittings of EIS data were calculated with EC-Lab (Demo version) software through the Randomize+Simplex method under 10000 iterations for Randomize and 5000 iterations for Simplex until a minimum chi-square (χ^2) value was obtained. All tests were repeated 3 times and their reproducibility was revealed. Afterward, the samples were ultrasonically cleaned and stored in a desiccator until post-corrosion SEM surface morphology observations.

RESULTS AND DISCUSSION

After the GTAW process, macro images taken from the cross sections of the weld joints with 110A, 140A, and 170A, respectively, are presented in Fig. 1. In macro examinations, especially in the weld seam, an increased porosity was determined with increasing welding current (110 to 170A). The first reason for the observation of porosity in the welding process can be the increase in the amount of supersaturated hydrogen in Al as a result of increased welding current [15]. On the other hand, since the obtained macro images were taken after etching in NaOH of the WZs, it is thought that these porosities may have been formed as a result of further etching of the weld seam. Moreover, it is predicted that the increased amount of welding current causes grain growth in the weld seam, so its sensitivity to NaOH etching solution may have increased [5]. Another finding is that in GTAW performed with 110A current, the visible area between base metal and weld seam disappears with increased welding current (Fig. 1a to 1c). It is thought that this may be due to the high Al content in the Al6013 alloy and the high thermal transfer coefficient (239 $W.m^{-1}.K^{-1}$) of Al

[25]. As a result of the increased welding current and the high thermal transfer coefficient, the heat transfers from the weld seam to the base metal and increases a homogeneous HAZ formation. It has been observed that this HAZ becomes more visible with increasing welding current (Fig. 1c). On the other hand, after the GTAW process in all different currents, pitting formation was observed especially in the middle of the v-groove (Fig. 1b). This is attributed to heat transfer from ER4047 to Al6013, which causes a partial cooling of the weld seam from the torch until it reaches the v-groove joint [21].

In Fig. 2, OM images of weld seams and HAZs after NaOH etching under different welding currents are presented. As the first striking finding, it is seen that with increased welding current grain size was increased especially in 170A. Moreover, as mentioned in Fig. 1, it is observed that the width of the HAZ increases with increasing current. It can be deduced that the increased welding current increases the width of the HAZ, but it causes an increase in the grain size of the weld seam, which may lead to a decrease in both the strength of the weld seam and more prone to corrosion.

EDX analysis results of WZs are presented in Fig. 3. The excess of Si element in the EDX analysis of the base metal is due to the wt.% 12 Si ratio of Al6013 (Table 1). On the other hand, even though the Cu amount seems low in the EDX analysis with #2, due to the wt.% 92.87 Al ratio of ER4047, it has a count of about 1K and is higher than base metal. The porosities of both base metal and weld seam were observed along with the SEM images and their elemental contents were confirmed by EDX analyses were taken. Another finding from EDX is that possible presence of elements that will form precipitation particles such as Al_2Cu and Mg_2Si in base metal and weld seams.

In Fig. 4, XRD analysis performed for determine possible precipitate phases that may occur in the microstructure of WZ before and after T6 heat treatment. As can be seen in Fig. 4a, characteristic Al peaks, which constitute the majority of both base metal and weld seam, were found at approximately 38, 44, 65, and 78 2Θ angles. With the T6 heat treatment, the Al peaks sharpened and the crystallinity of the microstructure increased. On the other hand, after T6 heat treatment, Al_2Cu precipitation phases were encountered at approximately 30, 37.5, and 51.3 2Θ angles, while Mg_2Si precipitation phases were encountered at 65.8, 72.4, and 79.1 2Θ angles (Fig. 4b). It is also predicted that these phases can be formed after welding with slow cooling and a long time in atmospheric conditions. Undoubtedly, this microstructural change will greatly affect corrosive properties. As a matter of fact, while the mechanical strength will increase with precipitation formation, the corrosive susceptibilities of the WZ may increase with possible galvanic couple formation.

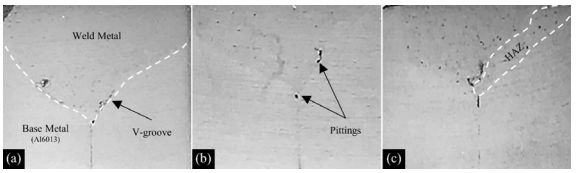

Figure 1. Macroscopic cross-section image of base metal, HAZ, and weld seams (a) 110A, (b) 140A, and (c) 170A

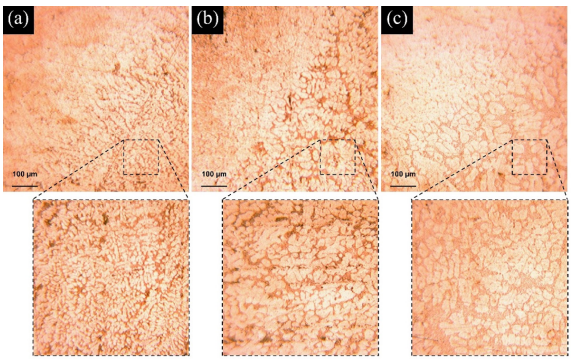

Figure 2. Optical microscopy of weld seams and HAZs, (a) 110A, (b) 140A, and (c) 170A

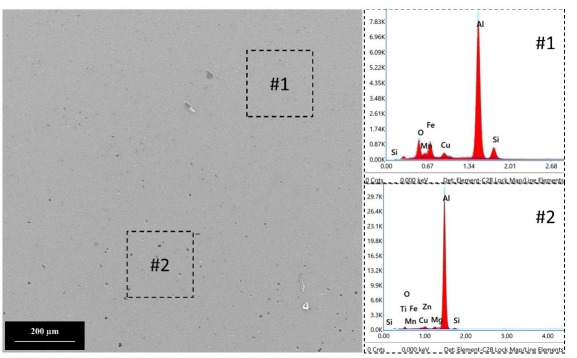

Figure 3. EDX analyses of weld zone which was welded with 170A

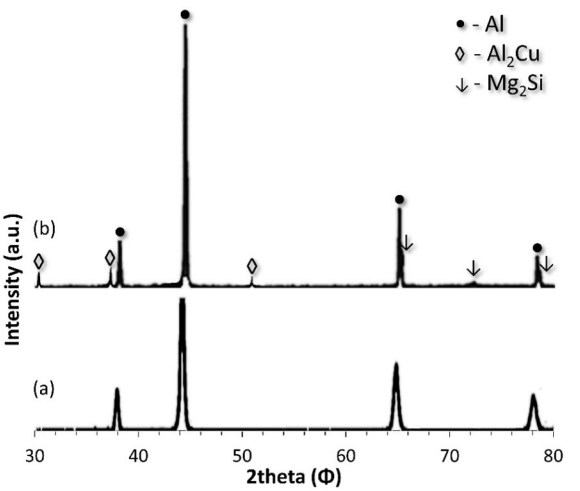

Figure 4. XRD results of 140A weld joints' WZ, (a) before and (b) after T6 heat treatment

The OCP test result of post-weld and T6 heat treated WZ is given in Fig. 5. As can be seen from Fig. 5a, while in the 110A and 170A joins became a steady state in a short time, this situation took about 600 s with the 140A. The size and distribution of the porosities in the weld seams and HAZs as a result of various welding currents are assumed to be the cause of this alteration. On the other hand, Fig. 5b, which shows the OCP change in the WZ after T6 heat treatment, a noble behaviour was observed in all samples up to about 900 s, while it became stable with increased immersion time. Particularly, the size, distribution and shape of the pores on the side of the weld seam are an important factor in the change of the open circuit potential (E_{ocp}) values before and after T6 heat treatment. The porosities formed on the surface may cause potential fluctuations along the surface as they form regions where the electrolyte remains stagnant during the increasing immersion time [26]. As a general opinion, it has been observed that the time for all samples to reach the steady state is 1200 s, and it can be said that the corrosion samples have a stable potential behaviour along their surfaces which indicates stable oxide film formation.

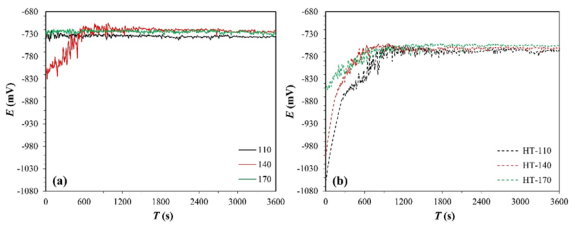

Figure 5. OCP immersion results of (a) post-weld and (b) T6 heat treated WZs

Fig. 6a and 6b represents PDS curves of post-weld and T6 heat treated WZ in 3.5% NaCl electrolyte after OCP are presented, respectively. In addition to PDS curves, the important corrosion parameters calculated by the Tafel extrapolarization method are presented in Table 2. Similar to the E_{ocp} values, the corrosion potential (E_{corr}) values in the PDS curves were observed in approximately the same potential range in all samples (-695 to -173 mV for post-weld and -752 to -755 mV for T6 heat treated). It can be deduced from the PDS curves corrosion current density (I_{corr}) of 170A (1.38 μA·cm^{-2}) was lower than the 110A and 140A samples (3.61 and 2.95 μA.cm^{-2}, respectively). As a matter of fact, since the I_{corr} value represents the amount of current passed per unit surface area in electrochemical tests, the decrease of this current means higher corrosion resistance or lower susceptibility of the sample [2,13]. On the other hand, the I_{corr} values of the HT-170A were increased (2.15 μA.cm^{-2}) after T6 heat treated WZ, while there was a decrease of HT-110A and HT-140A (2.08 and 2.40 μA.cm^{-2}, respectively). In other words, a decrease in I_{corr} values, i.e. increased corrosion resistance, was observed with the increasing welding current.

However, after T6 heat treatment, the corrosion behaviour of all samples showed similar behaviour. An increase in corrosion resistance occurred in the HT-110A sample. It is thought that this behaviour may have occurred as a result of the formation of porosity at the weld seams. This can be explained by porosity-precipitation relationship. Indeed, this situation can be explained as follows; decrease in I_{corr} of HT-110A was grain size and precipitation effect on grain boundaries [8,18]. As Çomaklı [27] mentioned, grain boundaries act as a physical corrosion barrier for coatings but uncoated samples used in present research behave differently due to the precipitations located in grain boundaries after T6 heat treatment. Furthermore, protective efficiency P (%) of the coating was described also with an equation: P (%) = [1 – (I_{corr}/I^0_{corr})] × 100 where I_{corr} and I^0_{corr} represent coating and substrate, respectively. But in this study, these parameters are specified as T6 heat treated and post-weld, respectively. In this way, 110A, 140A, and 170A P values were calculated as, 42.38%, 18.64%, and -55.79% respectively. So, it means that for 110A and 140A samples, T6 heat treatment was effective for corrosion protection while for 170A samples not. Moreover, calculated I_{corr} values are inversely proportional to the polarization resistance (R_p: Ω·cm^{-2}) values, and decreasing I_{corr} values indicate an increasing R_p value (Table 2). On the other hand, decreasing I_{corr} values change in direct proportion to the corrosion rate (*corr. rate*: μmpy) calculated by considering the homogeneous corrosion mechanism on the surface. In short, the increased corrosion resistance as a result of the decreasing I_{corr} value also decreases the corr. rate value and shows the homogeneous corrosion rate in μmpy unit that will degrade as a result of corrosion from the surface homogenously [28].

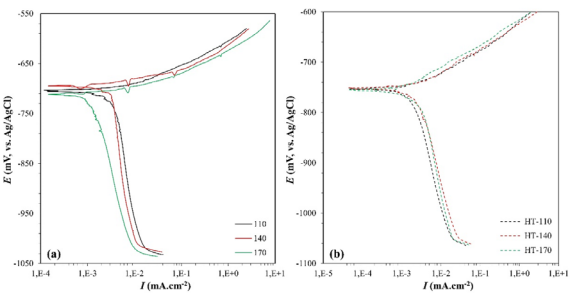

Figure 6. PDS curves of (a) post-weld and (b) T6 heat treated WZs

Table 2. Important corrosion parameters calculated from PDS curves according to Tafel extrapolation method

Samples	E_{corr} (mV)	I_{corr} (μA·cm^{-2})	β_a (V/decade)	β_c (V/decade)	R_p	corr.rate (μmpy)
110A	-704	3.61	0.04	0.61	4312	41.31
140A	-695	2.95	0.05	0.66	3078	25.97
170A	-713	1.38	0.03	0.40	8403	10.54
HT-110A	-753	2.08	0.05	0.36	9165	13.20
HT-140A	-752	2.40	0.05	0.30	7754	24.54
HT-170A	-755	2.15	0.05	0.29	8613	18.26

In Fig. 7, the EIS analysis results of the post-weld and T6 heat treated WZs are presented. Nyquist curves obtained from EIS analyses are evaluated as a measure of the stability of the oxide film on the samples in the electrolyte. From this point of view, the results of Nyquist curves are in parallel with the I_{corr} values obtained by the Tafel extrapolarization method from the PDS curves given in Fig. 6 and given in Table 2. In post-weld joints, the highest Zreal ($\Omega.cm^2$) vs Zimag ($\Omega.cm^2$) radius and thus the most stable oxide film characteristic and corrosion resistance were obtained with the 170A (Fig. 7a) [29]. Again, similar to the PDS curves, it was determined that HT-110A was more resistant to corrosion. However, unlike the PDS curves, it is observed that there is a greater increase in the Nyquist radii of the HT-110A, especially as the oxide film stability (Fig. 7c). As seen in Figs. 7a and 7c, it is thought that a flattening semi-circle curve in the Nyquist diagrams may have resulted from a possible capacitance behaviour [30]. Furthermore, due to various reasons such as surface homogeneity, roughness, porosity, and composition difference of the working electrode (WZs), the ideal capacitance behaviour can act as a constant phase element (CPE) [30]. On the other hand, it is seen in the bode diagrams given in Figs. 7b and 7d that both Freq (Hz) vs Zmod ($\Omega.cm^2$) and Freq (Hz) vs Zph (°) values diverge in the positive direction after T6 heat treatment. In order to determine the mechanism that triggers the oxide film formation and interactions between electrolyte, Nyquist curves should be investigated in terms of electrochemical circuit model.

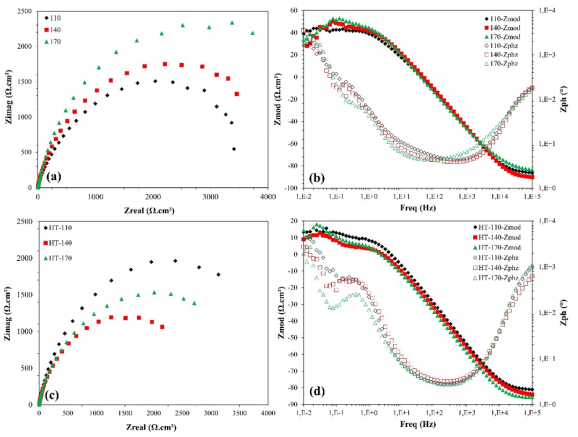

Figure 7. Non-destructive EIS results of (a) and (c) Nyquist diagram with (b) and (d) Bode-plots of WZs

In Fig. 8, the data fitting through the EC-Lab demo software using the data in the Nyquist diagrams presented in Figs. 7a and 7c, and the recommended equivalent circuit diagram are presented. The simulated fitting values are presented in Table 3. All results were well-fitted with the proposed two-constant equivalent circuit model [27]. Electrical components in the equivalent circuit are, R_E: resistance of the electrolyte, Q_P: constant phase element (CPE) of the passive film, R_P: resistance of the passive film, Q_{Pit}: constant phase element of pittings, and R_{Pit}: polarization resistance of associated with pits represent pits [24]. The Nyquist curves have presence of an element showing capacitive behaviour in the corrosion mechanism. However, this circuit element, which should show capacitive behaviour due to different reasons such as reactivity of surface, microstructural heterogeneity, roughness, and porosity on the weld seams, can act as a constant phase element (Q) [30]. The impedance of CPE is given by $Z_{CPE} = Q^{-1}(j\omega)^{-n}$, where Q is the magnitude of the CPE, $j^2 = -1$, ω is the angular frequency, and n (between 0 to 1) is the exponential term [30]. It's well known that for almost all Al and alloys protective and sticky oxide films occur on the surface with various environments [31]. So Q_P and R_P were the first important parameters for the corrosion protection of WZ. Lower Q_P indicates greater corrosion resistance and less ion absorption from the electrolyte by the passive film during immersion. The fact that the R_P increased as welding current increased (0.45, 14.59, and 928 for 110A, 140A, and 170A, respectively) indicates that the resistance of the passive oxide coating was enhanced. Additionally, as Sicupira et al. [30] pointed out, the diameter of the slope represents the charge transfer resistance, or, more specifically, the resistance of the passive film, and it is an indication that the corrosion resistance increased with a larger diameter of the slope. Here, it is thought that it may be due to the increase in the resistance of the oxide film due to the increase in the amount of Al diffused from base metal to weld seam with the increased welding current. Supporting this, the capacitance values of passive films, which is known as Q_P, are also decreased with increased welding current (32.53, 19.96, and 15.23 $F \times s^{(a_1-1)} \times 10^{-6}$ for 110A, 140A, and 170A, respectively). These values, which are valid for the passive film, coincide with the Tafel extrapolarization values obtained from the PDS curves for the samples after T6 heat treatment, and the corrosion resistance of the 110 increased after T6 heat treatment (R_P: 2684, 26.44, and 41.18 Ω and Q_P: 19.56, 57.12, and 22.51 $F \times s^{(a_1-1)} \times 10^{-6}$ for HT-110A, HT-140A, and HT-170A, respectively). As can be seen in the cross-sectional macro image (Fig. 1), similar results were observed for the R_{Pit} and Q_{Pit} values in the equivalent circuit [32], which occur due to the pittings seen especially in the weld seam. R_{Pit} values were calculated at 3075, 4751, 4808, 4562, 1923, and 3837 Ω for 110A, 140A, 170A, HT-110A, HT-140A, and HT-170A, respectively. On the other hand, Q_{Pit} values were calculated at 29.23, 13.18, 6.36, 11.00, 43.57, and 27.01 $F \times s^{(a_1-1)} \times 10^{-6}$ for 110A, 140A, 170A, HT-110A, HT-140A, and HT-170A, respectively. Here, more observable pittings on the 170A and HT-170A samples did not cause the RPit and Q_{Pit} trends to change. It is predicted that the grain size/structure, the size/number of the pittings, and the amount, size, and composition of precipitations (such as Al_2Cu, Mg_2Si, etc.) may have occurred as a result of the different welding currents.

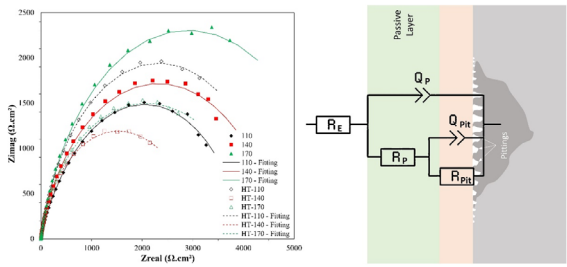

Figure 8. Fitting results of Nyquist diagrams with proposed equivalent circuit model on the surface of WZs

Table 3. Fitting parameters of the equivalent circuits with two time constants for Al6013 GTAW welded with ER4047 filler in 3.5% NaCl at room temperature presented in Fig. 8

Samples	R_E (Ω)	Q_P ($F \times S^{(a_1-1)} \times 10^{-6}$)	a_1	R_P (Ω)	Q_{Pit} ($F \times S^{(a_1-1)} \times 10^{-6}$)	a_3	R_{Pit} (Ω)
110A	1.414	32.53	0.89	0.45	29.23	0.76	3075
140A	2.115	19.96	0.88	14.59	13.18	0.82	4751
170A	2.470	15.23	0.74	928	6.36	0.98	5808
HT-110A	2.470	19.56	0.18	2684	11.00	0.93	4562
HT-140A	1.405	57.12	0.92	26.44	43.57	0.52	1923
HT-170A	2.045	22.51	0.90	41.18	27.01	0.88	3837

SEM images of corrosion defects occurring in HAZ after electrochemical corrosion tests of 110A, 140A, 170A, HT-110A, HT-140A, and HT-170A, respectively, are given in Fig. 9. It is thought that pitting corrosion occurs as a result of the cathode behaviour of the Al-Cu-Mg-Si precipitated particles at the grain boundary and acts as a cathode compared to the grain boundaries. In other terms, a galvanic couple occurs between precipitated particles and grain boundaries. In other words, pitting corrosion started with the presence of these precipitated particles at the grain boundaries. On the other hand, intergranular corrosion started on the surface and with the pitting corrosion continued a mixed corrosion mechanism [22]. Presumably, while intergranular corrosion will increase the pitting width, the pitting corrosion will also lead to deep corrosion with increasing immersion time [9]. In the post-corrosion SEM pictures of the samples that were post-weld, especially with the higher welding current, micropores that are inner walls of the pittings were not visible because of the rise in diffusion phenomena in the grains in the HAZ. A similar situation was observed in the post-corrosion SEM images of the HAZ of the T6 heat treated samples. So, as Braun [22] mentioned corrosion mechanism was independent of heat treatment for 6XXX Al alloys. With the exception of HT-170A, a relative decrease in the size of the pittings on the HAZ surface was seen after the T6 heat treatment. These pore sizes are compatible and supportive with the values specified in Fig. 8 and Table 3 and the equivalent circuit model. In T6 heat treated WZs, it was found that grain boundaries had a greater impact on corrosion as welding current increased. In other words, it was determined that the size of the pitting corrosion increased. The most important result that can be obtained from the post-weld SEM surface morphologies is that the increased welding current is quite effective in preventing pitting corrosion, which is a very dangerous type of corrosion [7,18]. Both PDS and EIS curves show that the corrosion resistance of the HT-110A increased. As shown in Fig. 9d, the pitting area has decreased, but it is anticipated that longer exposure time will increase the damage of pitting corrosion due to poor grain growth grain which caused by low welding current. This shows that it is very important to perform OM or SEM morphology examinations on surfaces after electrochemical corrosion measurements for detailed corrosion examination.

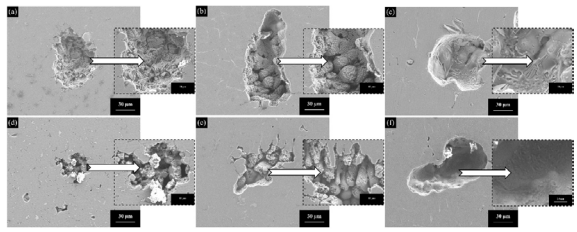

Figure 9. Post-corrosion SEM surface morphology investigation of WZs, (a, d) 110A, HT-110A, (b, e) 140A, HT-140A, and (c, f) 170A, HT-170A, respectively

CONCLUSION

In this study, Al6013 base metal was successfully joined with different welding currents by the GTAW method using ER4047 filler metal. To examine the effect of post-weld aging on different welds current, T6 heat treatment was carried out. The findings of the study can be summarized as follows;

- It was observed that the base metal and weld seam were tightly joined with all welding currents, and porosities were encountered on the weld seam with the increasing welding current. Furthermore, it has been predicted that the HAZ will expand with increasing welding current. Elemental compositions of both Al6013 and ER4047 were proved with EDX analyses. Al_2Cu and Mg_2Si precipitates were encountered in XRD results.

- The effects of both welding current and T6 heat treatment on the WZs are investigated with PDS tests. It was revealed that the corrosion resistance increased as the welding current increased (3.61, 2.95, and 1.38 $\mu A \cdot cm^{-2}$ for 110A, 140A, and 170A, respectively). However, with the T6 heat treatment, the corrosion resistance of 110A increased, surprisingly (3.61 to 2.08 $\mu A \cdot cm^{-2}$). This phenomenon is thought to be the result of increased Al diffusion from base metal to weld seam.

- Passive film characterization on WZs have been revealed with EIS tests according to both the Nyquist and Bode diagrams, as well as the proposed equivalent circuit

model. A two-constant equivalent circuit consisting of resistors and constant phase elements is recommended for all samples. Accordingly, it agrees with the proposed model that both a passive film is formed on the surface due to the Al and pitting occurs as a result of the different welding currents.

- Moreover, SEM surface morphology after corrosion tests confirmed that, pitting size and shape changes with various processes on weld seams, especially. It has been revealed that precipitates (such as Al_2Cu and Mg_2Si for Al alloys) that may occur in the microstructure during or after welding are very important in terms of corrosion susceptibilities. As a suggestion, it has been revealed that electrochemical methods do not give accurate results alone in corrosion measurements, moreover, surface morphology examinations such as OM or SEM can provide a more reliable result.

ACKNOWLEDGEMENT

The author would like to thank Professor Burak Dikici for helpful contribution on electrochemical corrosion tests..

CONFLICT OF INTEREST

Authors approve that to the best of their knowledge, there is not any conflict of interest or common interest with an institution/organization or a person that may affect the review process of the paper.

REFERENCES

1. Demirbaş K, Çevik S. TİG Kaynak Yöntemiyle Birleştirilmiş Alüminyum 1050 Alaşımının Mekanik Ve Mikroyapı Özellikleri, Academic Platform Journal of Engineering and Science, 2020 471–477.
2. Mercan E, Ayan Y, Kahraman N. Investigation on joint properties of AA5754 and AA6013 dissimilar aluminum alloys welded using automatic GMAW, Engineering Science and Technology, an International Journal, 23 (4) 2020 723–731.
3. Kosedag E, Ekici R. Low-velocity impact performance of B4C particle-reinforced Al 6061 metal matrix composites, Materials Research Express, 6 (12) 2019 126556.
4. Pantelakis SG, Daglaras PG, Apostolopoulos CA. Tensile and energy density properties of 2024, 6013, 8090 and 2091 aircraft aluminum alloy after corrosion exposure, Theoretical and Applied Fracture Mechanics, 33 (2) 2000 117–134.
5. Salah AN, Mabuwa S, Mehdi H, Msomi V, Kaddami M, et al., Effect of Multipass FSP on Si-rich TIG Welded Joint of Dissimilar Aluminum Alloys AA8011-H14 and AA5083-H321: EBSD and Microstructural Evolutions, Silicon, 14 (15) 2022 9925–9941.
6. Ayvaz M. Determination of the effect of artificial aging parameters on dry sliding wear resistance of 6013 aluminum alloy (Al-Mg-Si-Cu), International Advanced Researches and Engineering Journal, 5 (2) 2021 181–187.
7. Petroyiannis P V., Kermanidis AT, Papanikos P, Pantelakis SG. Corrosion-induced hydrogen embrittlement of 2024 and 6013 aluminum alloys, Theoretical and Applied Fracture Mechanics, 41 (1–3) 2004 173–183.
8. Barbosa C, Dille J, Delplancke J-L, Rebello JMA, Acselrad O. A microstructural study of flash welded and aged 6061 and 6013 aluminum alloys, Materials Characterization, 57 (3) 2006 187–192.
9. Braun R, Investigation on Microstructure and Corrosion Behaviour of 6XXX Series Aluminium Alloys, Materials Science Forum, 519–521 2006 735–740.
10. Haryadi GD, Kim SJ. Influences of post weld heat treatment on fatigue crack growth behavior of TIG welding of 6013 T4 aluminum alloy joint (Part 1. Fatigue crack growth across the weld metal), Journal of Mechanical Science and Technology, 25 (9) 2011 2161–2170.
11. Made Wicaksana Ekaputra I, Dwi Haryadi G, Mardikus S, Dewa RT. Probabilistic evaluation of fatigue crack growth rate for longitudinal tungsten inert gas welded al 6013-T4 under various postweld heat treatment conditions, E3S Web of Conferences, 130 2019.
12. He L, Zhang H,, Cui J. Effects of thermomechanical treatment on the mechanical properties and microstructures of 6013 alloy, Journal of Wuhan University of Technology-Mater. Sci. Ed., 24 (2) 2009 198–201.
13. Lei G, Wang B, Lu J, Wang C, Li Y, et al. Microstructure, mechanical properties, and corrosion resistance of continuous heating aging 6013 aluminum alloy, Journal of Materials Research and Technology, 18 2022 370–383.
14. Varshney D, Kumar K. Application and use of different aluminium alloys with respect to workability, strength and welding parameter optimization, Ain Shams Engineering Journal, 12 (1) 2021 1143–1152.
15. Li H, Zou J, Yao J, Peng H. The effect of TIG welding techniques on microstructure, properties and porosity of the welded joint of 2219 aluminum alloy, Journal of Alloys and Compounds, 727 2017 531–539.
16. Zhao Z, Liang H, Zhao Y, Yan K. Effect of Exchanging Advancing and Retreating Side Materials on Mechanical Properties and Electrochemical Corrosion Resistance of Dissimilar 6013-T4 and 7003 Aluminum Alloys FSW Joints, Journal of Materials Engineering and Performance, 27 (4) 2018 1777–1783.
17. Çetinkaya C, Tekeli S, Kurtuluş O. Alüminyum Alaşımlarının Kaynaklanabilirliği ve Kaynak Parametrelerinin Mekanik Özelliklere ve Mikroyapıya Etkisi, Politek Dergisi, 5 (4) 2002 321–335.
18. Abo Zeid EF. Mechanical and electrochemical characteristics of solutionized AA 6061, AA6013 and AA 5086 aluminum alloys, Journal of Materials Research and Technology, 8 (2) 2019 1870–1877.
19. Kosedag E, Ekici R. Low-velocity and ballistic impact resistances of particle reinforced metal–matrix composites: An experimental study, Journal of Composite Materials, 56 (7) 2022 991–1002.
20. Yürük A, Çevik B, Kahraman N. Analysis of mechanical and microstructural properties of gas metal arc welded dissimilar aluminum alloys (AA5754/AA6013), Materials Chemistry and Physics, 273 (March) 2021 125117.
21. Jeyaprakash N, Haile A, Arunprasath M. The Parameters and Equipments Used in TIG Welding: A Review, International Journal of Engineering Science, 2015 2319–1813.
22. Braun R. Investigations on the long-term stability of 6013-T6 sheet, Materials Charactarization, 56 (2) 2006 85–95.
23. ASTM International, ASTM G59 - Standard test method for conducting potentiodynamic polarization resistance measurements,

Volume 97, (West Conshohocken, PA, USA), 2014.
24. Mansfeld F. Electrochemical impedance spectroscopy (EIS) as a new tool for investigating methods of corrosion protection, Electrochima Acta, 35 (10) 1990 1533–1544.
25. Carvill J. Mechanical Engineer's Data Handbook, 1st ed., (Butterworth-Heineman), 1993.
26. Kartsonakis IA, Balaskas AC, Koumoulos EP, Charitidis CA, Kordas G. Evaluation of corrosion resistance of magnesium alloy ZK10 coated with hybrid organic–inorganic film including containers, Corrosion Science, 65 2012 481–493.
27. Çomaklı O. Improved structural, mechanical, corrosion and tribocorrosion properties of Ti45Nb alloys by TiN, TiAlN monolayers, and TiAlN/TiN multilayer ceramic films, Ceramics International, 47 (3) 2021 4149–4156.
28. Tozkoparan B, Dikici B, Topuz M, Bedir F, Gavgali M. Al-5Cu/B4Cp composites: The combined effect of artificially aging (T6) and particle volume fractions on the corrosion behaviour, Advanced Powder Technology, 31 (7) 2020 2833–2842.
29. Singh IB, Mandal DP, Singh M, Das S. Influence of SiC particles addition on the corrosion behavior of 2014 Al-Cu alloy in 3.5% NaCl solution, Corrosion Science, 51 (2) 2009 234–241.
30. Sicupira DC, Cardoso Junior R, Bracarense AQ, Frankel GS, de V. Electrochemical study of passive films formed on welded lean duplex stainless steel, Materials and Corrosion, 68 (6) 2017 604–612.
31. Dikici B, Topuz M. Production of Annealed Cold-Sprayed 316L Stainless Steel Coatings for Biomedical Applications and Their in-vitro Corrosion Response, Protection of Metals and Physical Chemistry of Surfaces, 54 (2) 2018 333–339.
32. Cabot PL, Garrido JA, Pe´rez E, Moreira AH, Sumodjo PTA, et al. Eis study of heat-treated Al-Zn-Mg alloys in the passive and transpassive potential regions, Electrochimica Acta, 40 (4) 1995 447–454.